ELSEVIER

Contents lists available at ScienceDirect

Tribology International

journal homepage: www.elsevier.com/locate/triboint





Friction and wear of a-C:H films deposited at different bias in air and NaCl solution

Cong Wang ^{a,b}, Xudong Sui ^{a,b,c}, Xiaolong Lu ^{a,c}, Xiao Zhang ^{a,c}, Zhen Yan ^{a,c}, Yan Lu ^{a,c,*}, Junying Hao ^{a,b,c,*}

- a State Key Laboratory of Solid Lubrication, Lanzhou Institute of Chemical Physics, Chinese Academy of Science, Lanzhou 730000, China
- b Center of Materials Science and Optoelectronics Engineering, University of Chinese Academy of Sciences, Beijing 100049, China
- ^c Qingdao Center of Resource Chemistry and New Materials, Qingdao 266000, China

ARTICLE INFO

Keywords:
A-C:H films
Substrate bias voltage
Friction
Electrochemical corrosion

ABSTRACT

a-C:H films were produced on 316 L stainless steel via magnetron sputtering technique. The effects of bias voltage on the composition, structure and properties of the films were studied. The sp^2C fraction grows as the bias voltage increases, and the internal stress and hardness increase constantly. In ambient air, the films deposited at -150 V have the lowest friction coefficient (COF) of 0.095, while those at -30 V have the lowest COF of 0.028 in salt solution, benefiting from the higher H content. The corrosion resistance of the film is affected comprehensively by the thickness, surface morphology, sp^2 clusters and transition layer. The a-C:H film at -60 V has the lowest corrosion current density (5.41 $\times 10^{-11}$ A/cm²) and the highest protection efficiency (99.8 %).

1. Introduction

Environment-affected maritime engineering equipment often fails prematurely owing to wear, corrosion, erosion and other factors, and faces the challenge of durability and safety [1,2]. The deposited a-C:H films, which have good lubricating capabilities, mechanical characteristics, and chemical inertness [3,4], can effectively prevent the damage that is caused to metal components by mechanical wear and saltwater corrosion, and these films can be employed as protective films in marine environments.

In the atmosphere, considerable chemical force and capillary force will be formed due to the existence of water and oxygen molecules. At the same time, when humidity level rises, a-C:H film friction coefficient progressively rises as a result of the increase of oxygen-containing groups on the friction surface [5,6]. In dry environment, a dense transfer film caused by the formation of $\rm sp^3$ sites is the key to ultra-low friction [7,8]. In an aqueous environment, low friction is achieved through the formation of hydrophilic hydrocarbon groups on the surface of films [9]. Overall, the excellent tribological features of a-C:H films are determined by the hardness, H content, and the amount of $\rm sp^2$ clusters. A higher level of hardness may effectively increase the load-bearing capacity of a-C:H films and lower the depth of wear marks, which leads to a

reduction in the amount of wear. Hydrogen in the film can passivate the dangling σ bonds, which in turn reduces the likelihood of covalent interactions and adhesion, avoiding the high friction generated during sliding [10–12]. Furthermore, the production of graphitized transfer film is aided by the greater sp^2C phase concentration, which in turn decreases the friction coefficient.

Besides the outstanding lubrication properties, the excellent corrosion resistance is another advantage for the utilization of a-C:H films in marine environments, because of the high hydrophobicity, chemical inertness, and low electrical conductivity [3,13,14]. However, the corrosion resistance of a-C:H films varies by the deposition techniques. Inevitably, pinhole flaws manifest themselves in the film during the magnetron sputtering deposition procedure [15], which results in the corrosion originating from the solution penetration. Also, the corrosion resistance of a-C:H films is significantly affected by the transition layer. The suitable transition layer contributes to the higher adhesion, avoiding the occurrence of delamination and reducing the formation of local defects [16-18]. In addition, the thickness can also influence the corrosion resistance of the film, since the corrosion process can be delayed by prolonging the corrosion path in thick films [19]. With these regards, the regulation of the composition and the microstructure is of significance to the corrosion resistance of the films besides the

E-mail addresses: luyan@licp.cas.cn (Y. Lu), jyhao@licp.cas.cn (J. Hao).

^{*} Corresponding authors at: State Key Laboratory of Solid Lubrication, Lanzhou Institute of Chemical Physics, Chinese Academy of Science, Lanzhou 730000, China.

tribological performance. In this sense, the control of substrate bias voltage is a convenient and effective way to tailor the tribological and anti-corrosion properties, because the H content, sp²/sp³-carbon bond ratio, compactness and thickness of the carbon films are all influenced by substrate bias and the transition layer can be also designed by changing substrate bias voltage.

This work therefore developed five distinct types of a-C:H films by magnetron sputtering on 316 L substrates with varying substrate bias voltage. The friction properties and corrosion behavior were investigated considering the influence by various bias voltage. The numerous properties of the a-C:H films are rationally explained by discussing factors such as H content, $\rm sp^2/\rm sp^3$ ratio, porosity, thickness, and transition layer.

2. Experimental details

2.1. The deposition of a-C:H films

The a-C:H films were deposited on 316 L stainless steel (25 mm \times 8 mm) and n-type Si (100) wafers (20 \times 20 mm) by PVD method. The test target is composed of a Cr target and two symmetrically distributed graphite targets. Sputtering gas Ar (99.9 %) and reactive gas CH₄ (99.9%) is introduced into the reaction during the preparation process. Ultrasound was used to clean the substrates for 15 min in petroleum ether and anhydrous ethanol to get rid of oil stains and other dirt on the surface, and then air-dried and put on a turntable in the deposition chamber. After the vacuum degree of the chamber reached to 3×10^{-5} Pa, with a high bias voltage (-400 V), the oxide layer and other impurities on the surface of Ar⁺ sputtering were used to complete the cleaning of the substrate for 30 min. The Ar flow rate was constant at 20 sccm during film deposition. A Cr metal layer of 4 A was deposited on the substrate for 7 min to promote bonding, and then the deposition of the Cr_xC_vH_z layer was started. The initial flow rate of CH₄ was 5 sccm, and gradually increased to 10 sccm at this stage. Cr target current drops to 0 A while C target current rises to 3.2 A, establishing a gradient process. In addition, since the initial process substrate bias is -60 V, the bias voltage also has a falling/maintaining/rising process during the deposition of the Cr_xC_vH_z layer, and it remains constant during the subsequent deposition of the a-C:H layer. Five distinct a-C:H films were made by varying the substrate bias. Table 1 outlines the deposition parameters. In order to convenience the discussion, the samples prepared under -30 V, -60 V, -90 V, -120 V and -150 V bias voltage were denoted as S1, S2, S3, S4 and S5.

2.2. Characterization

The surface and cross-sectional film morphology were obtained by the aid of field emission scanning electron microscopy (FE-SEMJSM-7610 F). The chemical structures were characterized by Raman (Raman HR Evolution) at a laser wavelength of 532 nm. X-ray photoelectron spectroscopy (ESCALAB 250Xi) was used for the elemental analysis, and the binding energy was calibrated with the C 1 s peak at 284.6 eV. To minimize the impact of the substrate, the hardness and modulus of the

films were studied using a nanoindenter with an indentation depth of 80 nm. By comparing the bending of the steel substrate before and after the test (FST1000), the internal stress of the a-C:H film was calculated using Eq. (1) [20]:

$$\sigma = \frac{E_s h_s^2}{6(1 - v_s)h_i} \left(\frac{1}{R_i} - \frac{1}{R_{i-1}}\right) \tag{1}$$

where Es is Young's modulus, vs is steel Poisson ratio; hs is the substrate thickness and hi is the coating; substrate's curvature, measured both before and after film deposition, is denoted by $R_{i\text{-}1}$ and R_i , respectively.

2.3. Friction and wear test

The dry friction properties of the samples in ambient air (40 \pm 5% RH and 25 \pm 2 °C) were tested with a reciprocating tribometer (CSM). The friction pair was a 9Cr18 steel ball (6 mm), and the friction is continued for 60 min under 5 N load and 5 Hz sliding frequency. The tribocorrosion performance test was carried out in a 3.5 wt% NaCl solution, the experimental setup (MFT-EC4000) is shown in the Fig. 1. Al₂O₃ ball (6 mm) was the friction pair. After the sample stood for 10 min, test was started with 5 N load and 0.5 Hz frequency. The wear scar morphology was observed by a 3D surface profiler (MicroXAM-800), also used to determine the wear volume. The wear rate is calculated by Eq. (2):

$$w = V/NS \tag{2}$$

where the wear rate $(mm^3/(Nm))$ is represented by w, V represents the wear volume (mm^3) , N is the load (N) and the total distance (m) is represented by S, respectively.

2.4. Electrochemical property

Electrochemical experiments were performed in a standard threeelectrode measurement system (CS 350). SCE is the reference electrode and Pt is the counter electrode. A sample with an exposed area of

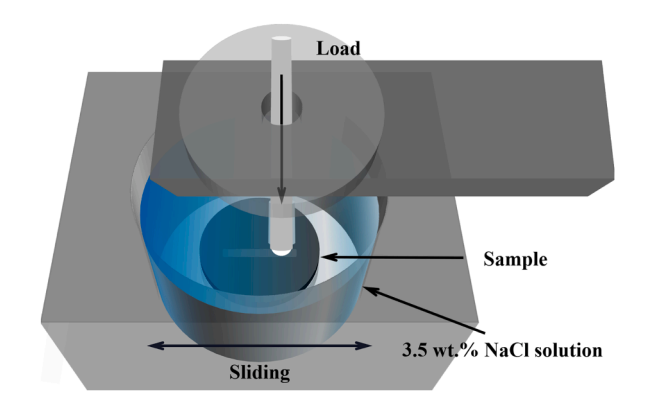


Fig. 1. Schematic diagram of friction device.

a-C:H films deposition parameters.

Process parameters	Cleaning	Film deposition							
		Cr	$Cr_xC_yH_z$	а-С:Н					
				S1	S2	S3	S4	S 5	
Ar flow (sccm)	20	20	20	20	20	20	20	20	
CH ₄ flow (sccm)	0	0	5→10	10	10	10	10	10	
Cr target current (A)	0.3	4	4→0	0	0	0	0	0	
C target current (A)	0.2	0	$0 \rightarrow 3.2$	3.2	3.2	3.2	3.2	3.2	
Bias (V)	-400	-60	-60→	-30	-60	-90	-120	-150	
Time (min)	30	7	30	150	150	150	150	150	

 1 cm^2 in saline is the working electrode. After 30 min of open-circuit potential stabilization, the Tafel tests were carried out at a scan rate of 1 mV/s throughout a scan range of -0.6-1.2 V.

3. Results and discussion

3.1. Structure and morphology

The surface and cross-sectional film morphology under a variety of substrate bias are shown in Fig. 2. The surface of the film becomes smoother as the bias voltage gets higher, and the size of the "island-like" structure that is present on the surface progressively gets smaller. Nevertheless, the surface of S1 sample is still uniform and dense under low substrate bias, and there is no microcrack propagation. The morphologies of the cross-section show that all a-C:H layers are amorphous and the thickness decreases with the increase of bias voltage. While the thickness of the Cr/Cr_xC_vH_z transition layer is gradually decreasing, more evident columnar development is emerging. The substrate bias can accelerate the movement of nearby positively charged ions to the sample, impact the surface, compensate for voids, and thus reduce surface roughness [21]. When the bias voltage is low, the energy of sputtering ions is weak, and the thermal effect that is created by the deposition process is minimal as well. In addition, the film is deposited at a fast pace, and the surface diffusion is not adequate to relieve the rapid buildup of local particle clusters, which results in a relatively rougher surface [22]. When the bias voltage is raised, the collision and bombardment of ions increased on the film surface. As a result, the sputtering and etching effects on the film surface are enhanced [23], the thermal effect is also increased, and the surface diffusion rate is improved, so the film thickness and surface roughness are significantly reduced. It is a similar mechanism that occurs during the deposition of the Cr/Cr_xC_vH_z transition layer, where the weakly bound C atoms are more likely to be bombarded and sputtered by high energy ions when the bias voltage is increased [24]. With the increase of Cr/C ratio, the transition layer changes from dense amorphous state to columnar structure [25,26]. Unlike the obvious columnar/amorphous interface of S5 sample, the a-C:H layer of S1 sample grows epitaxially on the basis of Cr/Cr_xC_vH_z layer, which makes the interface more compact.

D peak and G peak are two typical characteristic peaks of carbon

materials. In Raman spectrum analysis, the structural change of carbon film network can be judged by the ratio of the integral area of D peak to G peak and the half width of G peak [27,28]. Fig. 3a shows clearly that when the bias voltage is increased from -30 V to -150 V, the slope of the photoluminescence background of the a-C:H film diminishes. Because the background is closely related to the H content, the H content of the film can be estimated according to Eq. (3) [29]:

$$H(at.\%) = 21.7 + 16.6log \left[\frac{m}{I_G} (\mu m) \right]$$
 (3)

m is the slope of the fitted linear background, I_{G} is the intensity of the G peak.

The fitting data of Raman spectra and the calculation results of H content are shown in Fig. 3b. The I_D/I_G value of the a-C:H film grew as the bias voltage increased, indicating that the sp²C content in the film steadily increased. The half width of the G peak also shows a gradually increasing trend, indicating that the disorder of the film is gradually enhanced [27]. The phenomena above can be analyzed by ion implantation and bombardment. It can be known from the sub-implantation model of sputtered atoms and the atomic surface motion model [30, 31]. When high-energy particles are injected into the film, the released energy will increase the energy of local atoms, promote the transformation from stable sp²C bond to metastable sp³C bond, and increase the content of sp³C bond. The high-energy particles injected into the carbon film can also fill the gaps between the deposited atoms and improve the density. The bombardment impact of incident ions on the film surface is weaker at low bias voltage, and a large number of introduced H can not be released due to the rapid adsorption of hydrogen-containing ion clusters (-CH_n), resulting in higher sp³C bonds and H content [32]. After the bias is increased, the surface adsorption weakens, and the sub-implantation gradually dominates the growth, the higher ion bombardment energy leads to the increase of the lattice distortion and disorder effect of the film [33]. However, excessive heat generation will promote the re-conversion of sp³C bonds to sp²C bonds, resulting in the decrease of sp³ hybrid fraction [34]. At the same time, the bombardment of high energy ions will destroy the C-H-sp³ bond, resulting in the local recombination of H atoms, and the generated H₂ molecules migrate to the surface and desorb, resulting in the decrease of H content [35].

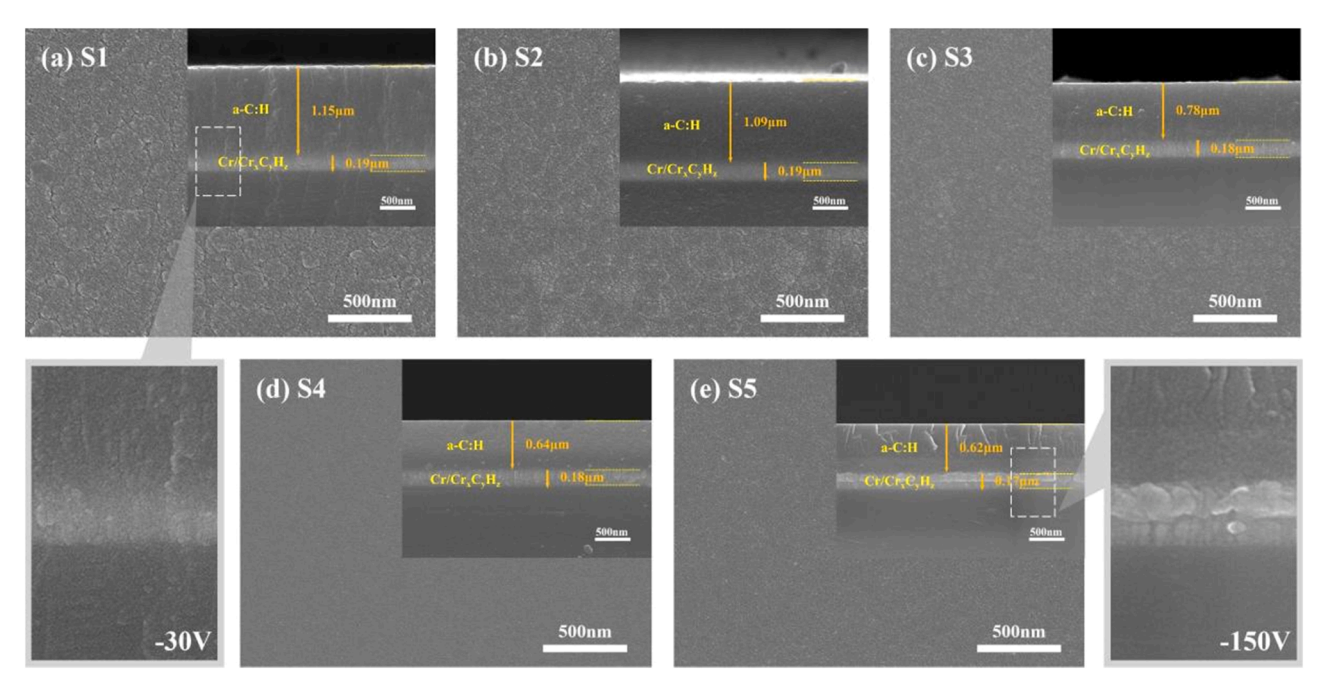


Fig. 2. Surface and cross-sectional film morphology under varied substrate bias.

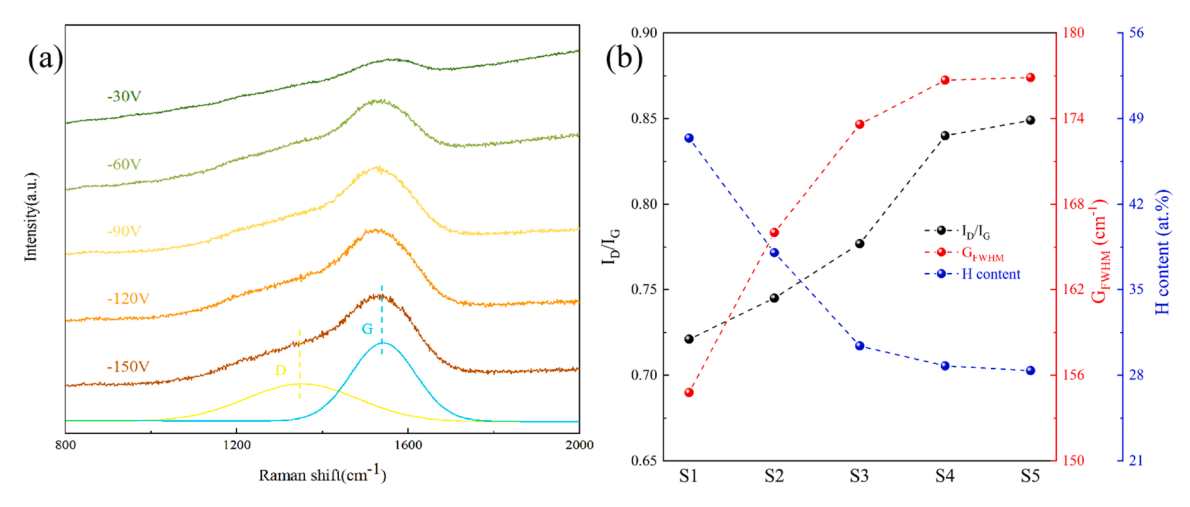


Fig. 3. (a) Raman spectra; (b) I_D/I_G , G_{FWHM} and H content of a-C:H films.

After 180 s of Ar $^+$ etching, the C 1 s spectra of a-C:H films were analyzed by XPS to validate the carbon bond state at a variety of substrate bias voltages. Fig. 4a indicates that the deconvolution XPS spectrum of the C 1 s peak has three major components: C-C sp 2 at 284.5 eV, C-C sp 3 at 285.2 eV, and C-O at 286.7 eV [28,36]. The C-O bond content of the a-C:H film is stable at about 5%, and the source may be the left-over oxygen in vacuum chamber or sample oxidation [37]. The ratio of sp 2 C and sp 3 C bonds in the film can be accurately estimated with the aid of the area ratio of the fitted peaks [38]. Fig. 4b illustrates the concentration of various carbon bonds inside a-C:H films. When the substrate bias voltage goes from - 30 V to - 150 V, the ratio of sp 2 /sp 3 increases from 0.65 to 1.61, indicating that the increase of substrate bias is beneficial to the transition from sp 3 C to sp 2 C. This is compatible with the preceding Raman findings.

3.2. Mechanical properties

Fig. 5 depicts the internal stress, hardness, and elastic modulus of a-C:H films under varied substrate bias. With a rise in substrate bias, the ion bombardment effect constantly increase, resulting in an increase in internal stress and hardness of the film. The results of Raman fitting show that I_D/I_G is on the rise, revealing the decrease of sp^3C in a-C:H film. Generally speaking, the content of sp^3C affects the hardness of DLC films, however, the ratio of I_D to I_G alone does not reflect the actual result of the film. The FWHM (G) results show that the high substrate bias will increase the lattice distortion and disorder effect of the films,

which will lead to higher strain distribution and film hardness [33,39, 40]. Besides, mechanical strength of a-C:H films rises with less bound H content or C-H bond fraction [41]. The higher H content greatly reduces the size of the annular $\rm sp^2$ structure, while contributing to the passivation of the dangling bonds on the film surface, resulting in the transformation of the C-C $\rm sp^2$ structure to the C-H $\rm sp^3$ structure. The large amount of C-H $\rm sp^3$ bonds lowers stress, steadily reducing the density and strain in the sample [18,42]. So, as the bias voltage gets higher, the H content decreases continuously, and the internal stress of the film cannot be effectively relieved, which is the decisive factor for the improvement of the hardness of the a-C:H film.

3.3. Friction and wear test

3.3.1. In ambient air

The friction curves of a-C:H films in ambient air are shown in Fig. 6a. The friction coefficient of all films is found to have a run-in period, which is reduced with an increase in the substrate bias. The friction coefficient of S1 sample is as high as 0.23 and the sample were worn through in the later stage of the experiment. The friction coefficient continuously lowers when the bias voltage is raised, which was caused by the decrease of the H/C ratio in a-C:H film [5]. In the process of friction, oxygen and water vapor in air react on sliding surfaces to form oxygen-containing groups [8], resulting in chemical and capillary force [11,12]. At the same time, the interaction of hydrogen bonds between the groups will also increase the friction coefficient during the sliding

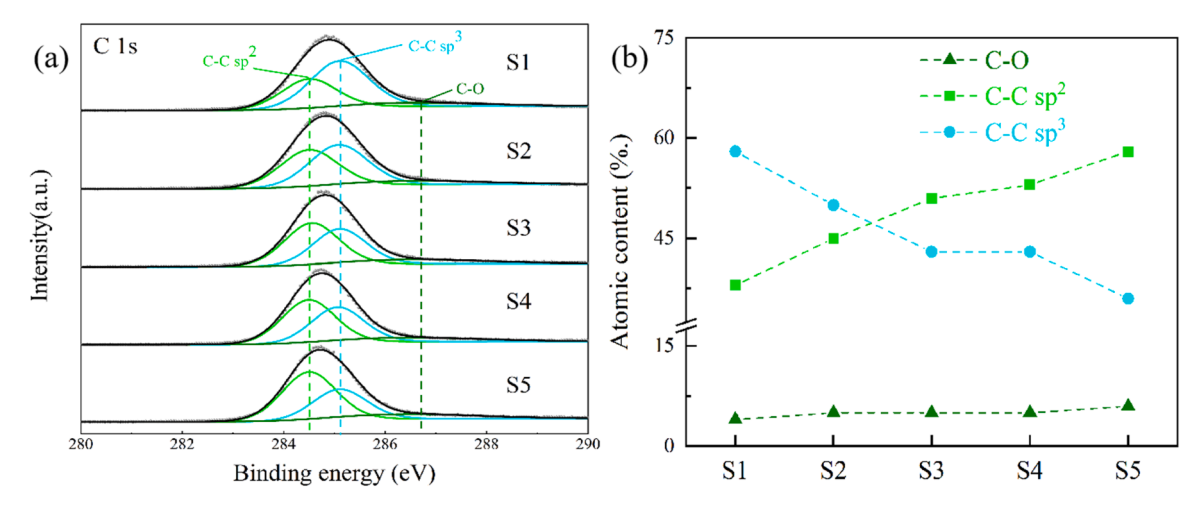


Fig. 4. Changes of (a) C 1 s spectra; (b)chemical bonding under varied substrate bias.

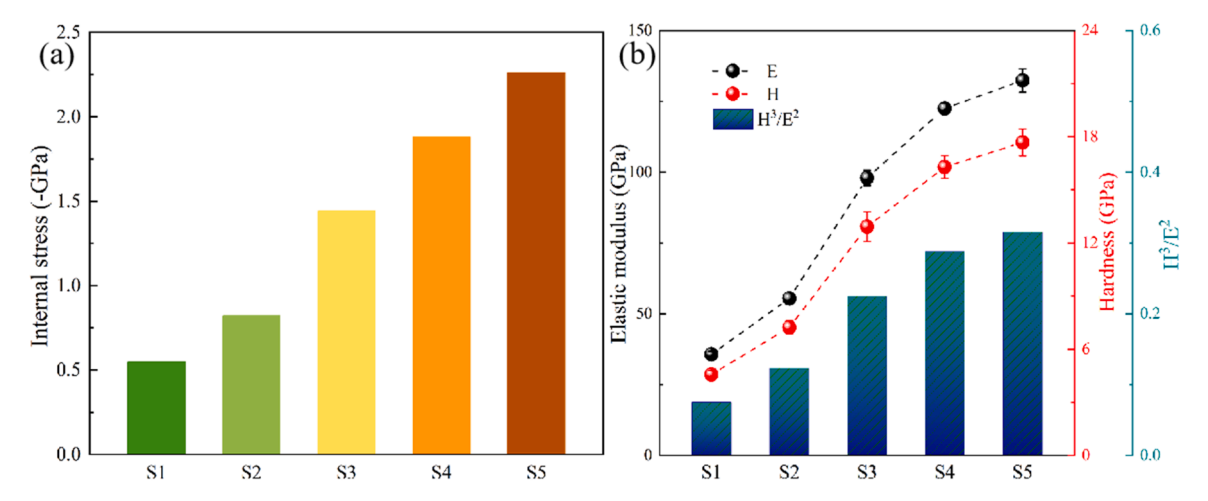


Fig. 5. (a) Internal stress; (b) Hardness; Elastic modulus and H³/E² of a-C:H films under varied substrate bias.

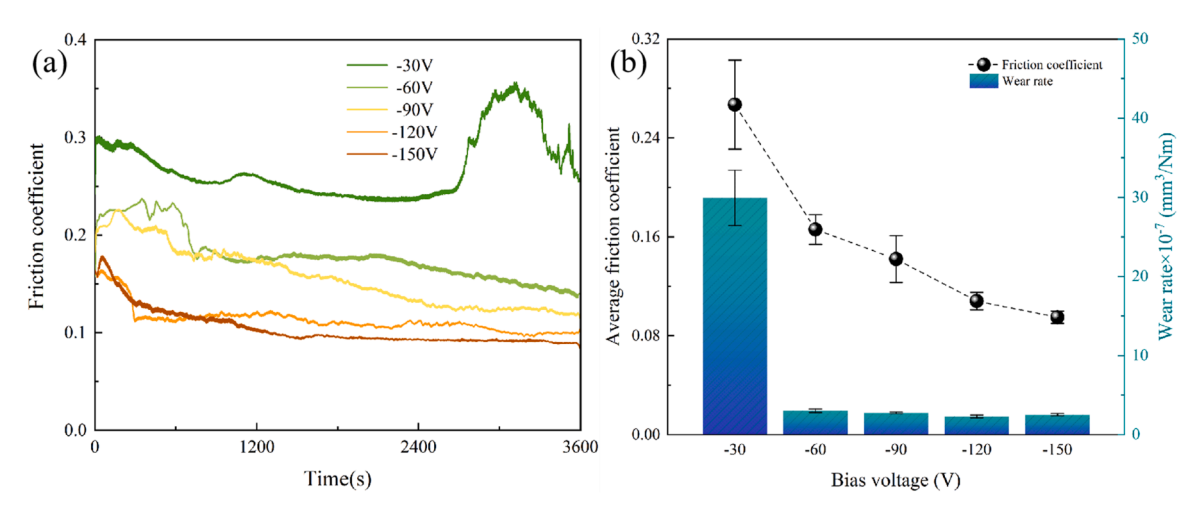


Fig. 6. (a) Friction curves; (b) average friction coefficient and wear rate of a-C:H films in ambient air.

process [6]. As bias voltage rises, the unsaturated -CH bond decreases and the number of oxygen containing groups formed by oxidation decreases, which is beneficial to the shortening of the run-in period and the decrease of friction coefficient [43]. In addition, higher sp 2 C content is also advantageous for the formation of graphitized transfer film during friction. The stable friction coefficient and wear rate of the film are shown in Fig. 6b, and a reduction in the wear rate is seen when the bias voltage is raised. This is because the hardness and $\rm H^3/E^2$ value of the film are improved, and the resistance to plastic deformation is enhanced [44]. However, the wear rate of a-C:H films under different bias voltages is not monotonous. The minimum wear rate of 2.29 \times 10 $^{-7}$ mm $^3/Nm$ at - 120 V bias is slightly increased to 2.52 \times 10 $^{-7}$ mm $^3/Nm$ at - 150 V. This may be related to the decline of H content and the rise of sp 2 C content, which leads to the occurrence of adhesion phenomenon.

The film marks on the sample surface and 9Cr18 steel ball are analyzed, and the experimental outcomes are shown in the Fig. 7. Fig. 7 (a)-(c) illustrates the SEM morphology of the steel balls. The findings indicate that the wear scar region of sample S1 is enormous, that a substantial quantity of wear debris has collected around it, and that the transfer layer on the surface of the steel ball is loose and discontinuous. Although the transfer layer of S3 and S5 samples are still discontinuous, the adhesion area increases, indicating the increase of graphitization in the friction process. Fig. 7(d)-(f) shows the wear scars and 3D morphologies of a-C:H film after friction test. The wear scar exhibits the characteristic morphology of abrasive wear, with a prominent furrow effect. The S1 sample has been worn through and the wear scar depth

exceeds the total thickness of the film, while the S3 and S5 samples have a shallower wear scar depth. This is because the hardness of the film increases gradually. Additionally, the load-bearing capacity increases, so that the depth of wear scar decreases. Significant plastic deformation is found on both sides of the wear scar, which is caused by the high contact stress in the friction process [45]. S5 samples have a greater furrow effect than S3 samples, which may be attributed to the decreasing H concentration in the a-C:H film when the bias voltage is increased. In this case, the σ bond produced by the film itself or mechanical wear cannot be effectively passivated, thus causing a strong adhesion in the sliding process [3,46].

3.3.2. In 3.5 wt% NaCl solution

Fig. 8a displays the tribological parameters of an a-C:H film immersed in 3.5 wt% NaCl solution, which are significantly different from the friction experienced in air. It can be clearly seen that the S1 sample exhibits relatively excellent lubrication performance. For different samples, the performances of the a-C:H films in the early stage of the friction are different. The friction coefficient diminishes continually in S1, S2 samples. The friction coefficient of the S3 sample also decreased, but reached a stable stage after a short run-in period. Different from the samples above, the friction coefficients of S4 and S5 samples first increased and then decreased. However, the friction coefficient of all samples in the later stage of the test is basically the same, about 0.045, suggesting good lubricity. Fig. 3b clearly demonstrates that the S1 and S2 samples have a higher H content, which can effectively

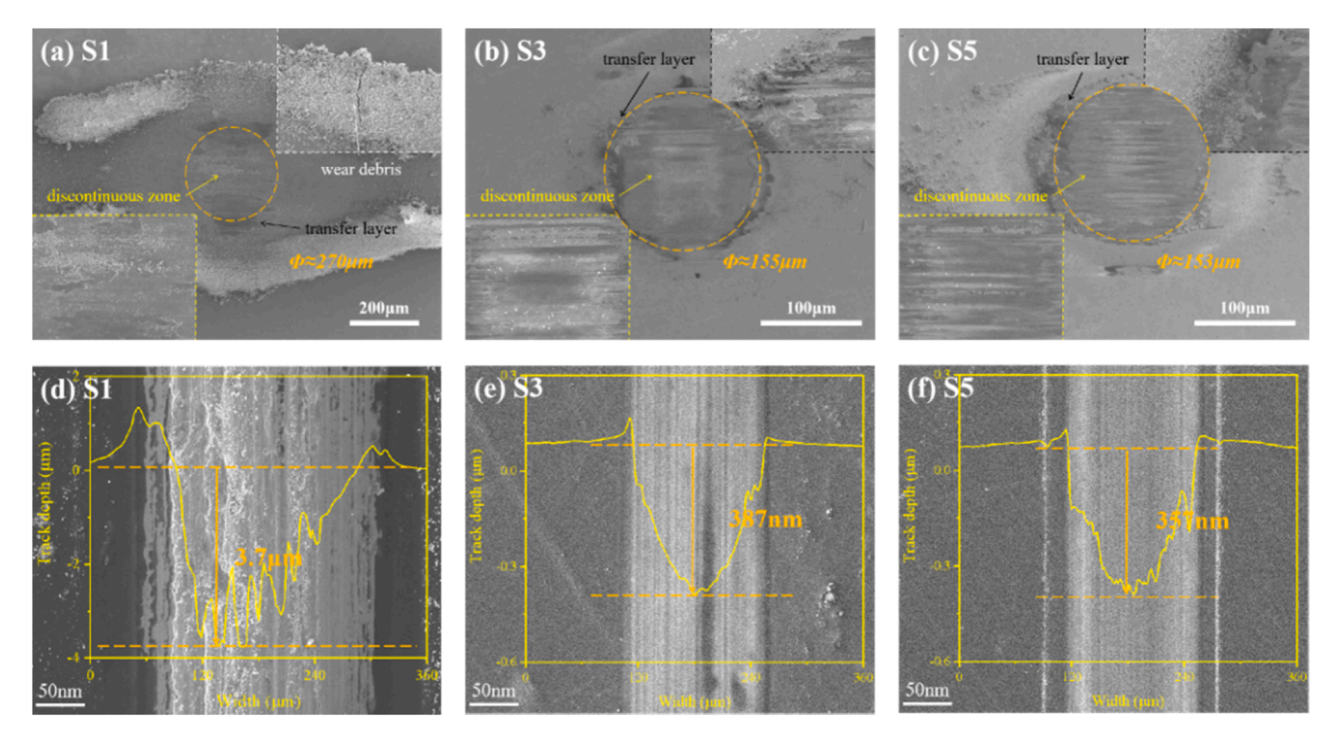


Fig. 7. SEM of (a-c) the steel balls; (b) wear scars and 3D morphologies of a-C:H films.

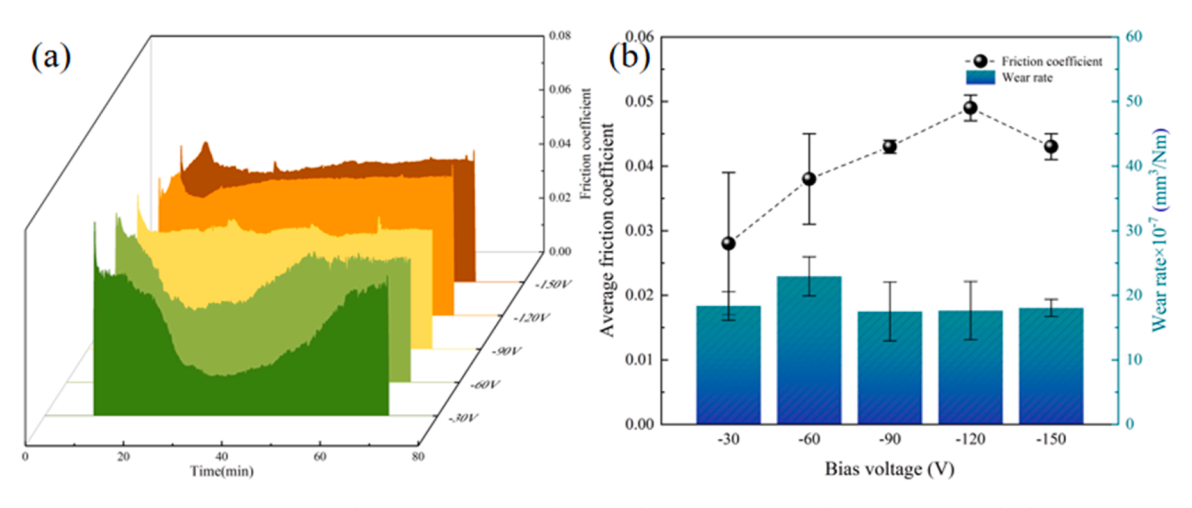


Fig. 8. (a) Friction curves; (b) average friction coefficient and wear rate of a-C:H films in 3.5 wt% NaCl solution.

passivate the unoccupied or free σ bonds on the surface of the a-C:H film [11]. Furthermore, due to the existence of a mass of free H inside the film, the H atoms lost during the sliding process can be replenished, terminating those σ bonds that may be exposed due to mechanical wear or thermal desorption, which provides additional passivation to the film surface, reducing the possibility of adhesion [10,47]. With the progress of friction, the H stored in the film is continuously consumed and the friction force increases, so the S1, S2 sample shows a friction coefficient curve which decreases at first and then increases. However, because of the low H content on the surface, more σ bonds produced by S4, S5 film during the friction process, resulting in strong covalent bond interactions, so the friction coefficient increases in the early stage. In addition, during the friction process, the C-CH bond is broken up by mechanical action and reacts with water molecules, and the carbon atoms are combined with H atoms and OH groups generated by the dissociation of water molecules, reducing friction through the formation of hydrophilic hydrocarbon groups [9,48]. Fig. 8b shows the stable friction coefficient and wear rate of a-C:H film in salt solution. Under

different bias voltage, the wear rate of the films are almost the same, fluctuating around $1.8\times10^{-6}~\text{mm}^3/\text{Nm}.$ Only the S2 sample has a slightly higher wear rate. When the substrite bias is lower, the film has higher H content, which can effectively reduce the adhesion, but lower hardness and less ability to resist frictional shearing forces. Even though the hardness of the film becomes harder as the bias voltage gets higher, fewer hydrocarbon groups were formed on the surface of the film, resulting in greater wear at the beginning of the test. These reasons above jointly affect the wear rate of a-C:H films.

Fig. 9 shows the 3D wear scar morphologies and cross-section curves of S1 and S5 samples. For S1 samples (Fig. 9(a), (b)), the furrow effect is more obvious on the surface of the a-C:H film, which is attributable to the soft surface of the film cutted by abrasive debris generated during the rubbing process, indicating that abrasive wear is the main wear mechanism. The hardness of the S5 sample is higher than that of the S1 sample and a relatively smooth wear scar surface is generated. However, due to the weak interaction between Al and graphite, the transfer film cannot be attached to the Al_2O_3 ball, resulting in the increase of wear

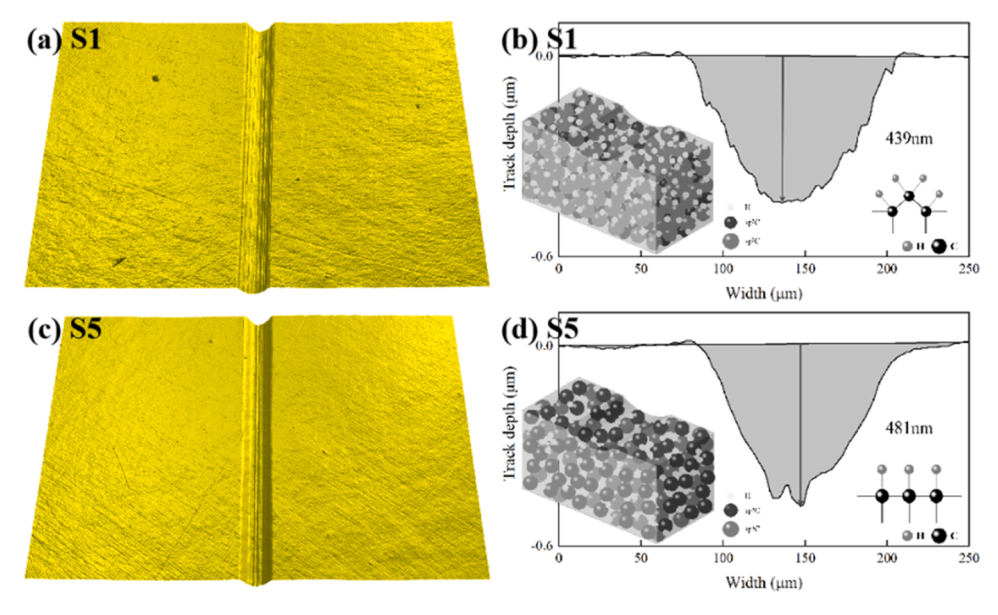


Fig. 9. 3D wear scar morphologies and cross-section curves of S1 (a,b) and S5 (c,d) samples.

debris [49]. Especially in salt solution, owing to the fluidity of the water, the wear debris is easier to migrate back to the friction surface [50], causes the generation of grooves at the bottom of the wear scar. On the basis of the results above, the composition diagrams of S1 and S5 samples are constructed as shown in Fig. 9(b), (d). Compared with S5 sample, S1 sample have relatively fewer sp²C content and smaller cluster size, and there are more sp³C and H in the thin films. Except for majority the hydrogen atoms paired with σ bonds, there are more free H in the films in the form of molecules or atoms. In addition, there are also partially double-hydrogenated surface carbon atoms, which further increase the hydrogen density on the surface of the a-C:H film, providing better shielding or passivation [12]. It is precisely because of these differences in composition that S1 sample shows relatively better tribological properties in salt solution.

3.4. Electrochemical behaviors

The previous reports have shown that the synergistic effect of friction and corrosion accelerates the local exfoliation and failure of the film [51, 52]. In contrast, the wear scar of the a-C:H films that was detected during the prior corrosion-friction test was shallow, without obvious pitting or spalling, which indicates that the film possess strong resistance

to corrosion. So, in order to evaluate the corrosion behavior of a-C:H films in 3.5% NaCl solution, the electrochemical performance tests were conducted. Fig. 10a shows the potentiodynamic polarization curves of 316 L stainless steel and a-C:H films under different bias voltages. In contrast to 316 L stainless steel, the corrosion potential of a-C:H films rises, whilst the corrosion current density falls, which manifests a good anti-corrosion effect. It is clear from Fig. 10 that the polarization curve of S5 sample is similar to that of the bare 316 L substrate, accompanied by the occurrence of pitting corrosion. In addition, obvious pitting corrosion also occurred in S1 sample. In contrast, the S2, S3, and S4 samples showed better corrosion resistance.

The electrochemical corrosion resistance of the films was determined by calculating the corrosion potential (E_{corr}) and corrosion current density (j_{corr}) using the Tafel extrapolation technique, and calculate their polarization resistance (Rp) by Eq. (4) [53]:

$$R_p = \frac{\beta_a \times \beta_c}{2.303i_{coor}(\beta_a + \beta_c)} \tag{4}$$

Where β_a and β_c is the anodic and cathodic Tafel slope. The calculation results are shown in Table 2. After the deposition of the a-C:H film, the corrosion current density of the 316 L substrate decreased by about two orders of magnitude. With the increase of substrate bias, the

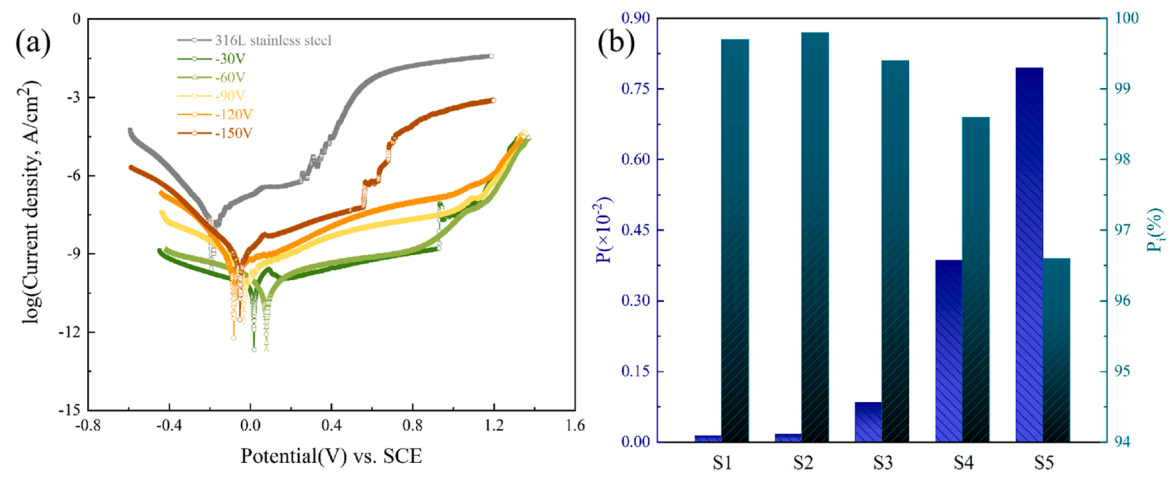


Fig. 10. (a) Potentiodynamic polarization curves; (b) porosity (P) and protective efficiency (Pi) of bare 316 L and a-C:H films coated in 3.5 wt% NaCl solution.

Table 2Sample electrochemical parameters.

Samples	E _{coor} (V)	I _{coor} (A/cm ²)	β _a (V/decade)	β _c (V/decade)	R_p (Ωcm^2)
316 L steel S1	-0.194 0.027	2.72E-08 5.79E-11	0.233 0.079	0.110 0.442	1.20E+ 06 1.00E+ 09
S2	0.077	5.41E-11	0.268	0.243	5.00E + 08
S3	-0.010	1.76E-10	0.235	0.149	2.30E + 08
S4	-0.074	3.78E-10	0.395	0.104	9.50E+ 07
S5	-0.057	9.18E-10	0.208	0.137	3.90E+ 07

polarization resistance decreased continuously, indicating that the corrosion resistance of the a-C:H film was weakened.

Because there are a few pinhole defects in the a-C:H film, the corrosive electrolyte will infiltrate along the defects and cause local corrosion. Therefore, the quantitative analysis of film porosity is particularly important. According to the electrochemical parameters of the substrate and the film, the porosity (P) of the film can be calculated by Eq. (5) [54]:

$$P = \frac{R_P(Substrate)}{R_P(Film/Substrate)} \times 10^{-|\Delta E_{coor/\beta_a}|}$$
 (5)

where ΔE_{coor} is the difference in corrosion potential between the substrate and the film covered substrate, β_a represents the slope of the anodic Tafel on the substrate. In Eq. (6), the corrosion current density of the substrate (i_{coor}^0) and the film-coated substrate (i_{coor}) can also be utilized to calculate the film protective efficiency (P_i) [55]:

$$P_i = 100 \left(1 - \frac{i_{coor}}{i_{coor}^0} \right) \tag{6}$$

The calculation results are shown in Fig. 10b. The porosity of the film constantly increases as the bias voltage is raised, exposing more of the substrate to the corrosive solution, and the protection efficiency decreases.

The cross-section image in Fig. 2 indicates that all a-C:H layers under different substrate bias exhibit dense amorphous structures, which is beneficial to the improvement of the corrosion resistance of a-C:H films. The a-C:H film formed under low substrate bias is relatively thicker and thus has a longer corrosion path, which can delay the occurrence of corrosion. In addition, the a-C:H film has a large H content under low bias, and H atoms can promote the conversion of $\rm sp^2C$ to $\rm sp^3C$ on the surface of the film, forming the dangling bonds of the surface configuration. The reaction between adjacent dangling bonds will form a new $\rm sp^3$ carbon bond, which promotes the formation of a dense carbon network on the surface of the film and plays a good sealing effect [56]. However, the surface of the sample is rougher at low bias voltage and the size of the "island-like" structure is larger, which provides more active sites for triggering the electrochemical corrosion reaction and promotes

the occurrence of corrosion [57,58]. It has been shown by Raman and XPS research that when substrate bias is increased, the $\rm sp^3C$ content of a-C:H films falls and the $\rm sp^2C$ content rises. Due to the fact that $\rm sp^2$ hybridization is more favorable to electronic conduction, the formation of electron transport channels by $\rm sp^2$ hybridization makes the electrochemical corrosion response more severe [59]. Moreover, the corrosion resistance of a-C:H film was also enhanced by the reduced residual stress [60]. Besides the dense layer, the transition layer also has a great influence on the corrosion resistance of a-C:H film [18]. The SEM pictures clearly show that when the substrate bias is increased, more obvious columnar growth was observed in the $\rm Cr/Cr_x C_y H_z$ transition layer, which would lead to the generation of more microcracks and defects, increasing electrolyte penetration and corrosion response.

According to the analysis above, the schematic diagram of pitting corrosion mechanism for S1 and S5 samples is shown in Fig. 11. Compared with the S5 sample, the thicker a-C:H layer of the S1 sample prolonged the corrosion path and postponed the occurrence of pitting corrosion. When the substrate bias voltage is - 30 V, the deposited a-C: H films have higher surface roughness, which provides more active sites and leads to the occurrence of pitting corrosion. When the substrate bias voltage is - 150 V, the number and size of $\rm sp^2$ clusters increase, which promotes the charge transfer. At the same time, many pore defects in the $\rm Cr/Cr_xC_yH_z$ transition layer also promote the penetration of the solution, which deteriorates the corrosion resistance of S5 samples, leading to the aggravation of pitting corrosion.

4. Conclusion

In order to meet the demand of lubrication requirements in marine environment, the a-C:H films with outstanding tribological properties were developed by PVD under different substrate bias. By adjusting the substrate bias voltage, the composition, microstructure, friction performance and corrosion resistance of the film can be tailored in a convenient way. The influences by substrate bias on the performances of the film were evaluated and studied systematically.

An increase in the substrate bias leads to an enhancement in the sputtering and etching effects, as well as a reduction in the surface roughness and thickness of the a-C:H film. The C-H bond was broken as a result of the bombardment with high-energy particles and escaped as H_2 , which resulted in a decrease in the amount of hydrogen contained in the film. In addition, an excessive amount of heat encourages the change of ${\rm sp^3C}$ to ${\rm sp^2C}$, which increases the graphitization of the thin films. Because of the rise in bombardment energy and the reduction in the amount of hydrogen present, both the internal stress and the hardness of the films increased continuously. The tribological properties of a-C:H films in ambient air and in saline solution are significantly different. In the ambient air, it has been shown that the friction coefficient decreases constantly as the substrate bias increases, reaching a value as low as

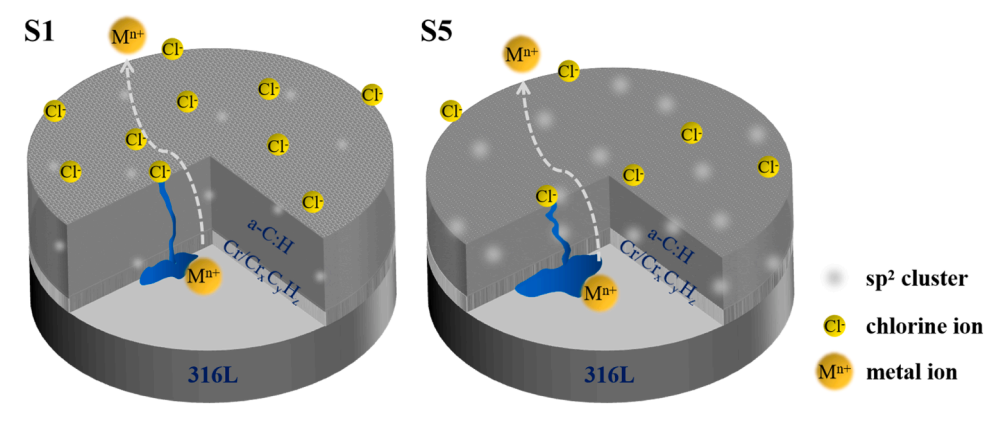


Fig. 11. Schematic diagram of pitting corrosion mechanism for S1 and S5 samples.

0.095 at a bias of - 150 V. During this procedure, the friction is mostly determined by chemical force, capillary force, and oxygen-containing groups. The tribological characteristics follow the opposite pattern in a 3.5 wt% NaCl solution, in which the lowest average friction coefficient of 0.028 emerged at the bias of - 30 V. Except for the S1 sample that provides more active sites due to the rough surface and the S5 sample that has a high $\rm sp^2$ content and a columnar growth of the transition layer, no pitting potential was found in the Tafel test for the rest of the samples. After the deposition of the a-C:H film, the corrosion current density of the samples dropped by 2–3 orders of magnitude in comparison to the 316 L substrate. Among them, the S2 sample has the lowest corrosion current density (5.41 $\times 10^{-11} \rm A/cm^2)$ and the highest protection efficiency (99.8%), exhibiting excellent corrosion resistance.

Declaration of Competing Interest

The authors declare that they have no known competing financial interests or personal relationships that could have appeared to influence the work reported in this paper.

Data Availability

Data will be made available on request.

Acknowledgments

This work was supported by the National Natural Science Foundation of China (grant number 51835012 and 51975554), the Natural Science Foundation of Gansu Province (21JR7RA081), Basic Research Project (2020-JCJQ-ZD-155-12) and CAS "Light of West China".

References

- [1] Yang G, Ying L, Haichao L. Experimental studies on the local corrosion of low alloy steels in 3.5% NaCl. Corros Sci 2001;43:397–411.
- [2] Soares CG, Garbatov Y, Zayed A, Wang G. Influence of environmental factors on corrosion of ship structures in marine atmosphere. Corros Sci 2009;51:2014–26.
- [3] Erdemir A, Donnet C. Tribology of diamond-like carbon films: recent progress and future prospects. J Phys D Appl Phys 2006;39:R311–27.
- [4] Wu G, Dai W, Zheng H, Wang A. Improving wear resistance and corrosion resistance of AZ31 magnesium alloy by DLC/AlN/Al coating. Surf Coat Technol 2010;205:2067–73.
- [5] Sánchez-López JC, Erdemir A, Donnet C, Rojas TC. Friction-induced structural transformations of diamondlike carbon coatings under various atmospheres. Surf Coat Technol 2003;163–164:444–50.
- [6] Li H, Xu T, Wang C, Chen J, Zhou H, Liu H. Tribochemical effects on the friction and wear behaviors of a-C:H and a-C films in different environment. Tribology Int 2007;40:132–8.
- [7] Manimunda P, Al-Azizi A, Kim SH, Chromik RR. Shear-induced structural changes and origin of ultralow friction of hydrogenated diamond-like carbon (DLC) in dry environment. ACS Appl Mater Interfaces 2017;9:16704–14.
- [8] Li H, Xu T, Wang C, Chen J, Zhou H, Liu H. Humidity dependence on the friction and wear behavior of diamond-like carbon film in air and nitrogen environments. Diam Relat Mater 2006;15:1585–92.
- [9] Wu X, Ohana T, Tanaka A, Kubo T, Nanao H, Minami I, et al. Tribochemical investigation of DLC coating tested against steel in water using a stable isotopic tracer. Diam Relat Mater 2007;16:1760–4.
- [10] Bernal RA, Chen P, Schall JD, Harrison JA, Jeng Y-R, Carpick RW. Influence of chemical bonding on the variability of diamond-like carbon nanoscale adhesion. Carbon 2018;128:267–76.
- [11] Erdemir A. The role of hydrogen in tribological properties of diamond-like carbon films. Surf Coat Technol 2001;146–147:292–7.
- [12] Erdemir A. Genesis of superlow friction and wear in diamondlike carbon films. Tribology Int 2004;37:1005–12.
- [13] Paul R, Das SN, Dalui S, Gayen RN, Roy RK, Bhar R, et al. Synthesis of DLC films with different sp2/sp3ratios and their hydrophobic behaviour. J Phys D: Appl Phys 2008:41.
- [14] Miyagawa S, Nakao S, Choi J, Ikeyama M, Miyagawa Y. Effects of target bias voltage on the electrical conductivity of DLC films deposited by PBII/D with a bipolar pulse. Nucl Instrum Methods Phys Res Sect B Beam Interact Mater At 2006; 242:346–8.
- [15] Panjan P, Čekada M, Panjan M, Kek-Merl D, Zupanič F, Čurković L, et al. Surface density of growth defects in different PVD hard coatings prepared by sputtering. Vacuum 2012;86:794–8.

- [16] Zhu H, Ma L, Liu N, Wei Q, Wu D, Wang Y, et al. Improvement in anti-corrosion property of hydrogenated diamond-like carbon film by modifying CrC interlayer. Diam Relat Mater 2017;72:99–107.
- [17] Azzi M, Amirault P, Paquette M, Klemberg-Sapieha JE, Martinu L. Corrosion performance and mechanical stability of 316L/DLC coating system: Role of interlayers. Surf Coat Technol 2010;204:3986–94.
- [18] Marin E, Lanzutti A, Nakamura M, Zanocco M, Zhu W, Pezzotti G, et al. Corrosion and scratch resistance of DLC coatings applied on chromium molybdenum steel. Surf Coat Technol 2019:378.
- [19] Uematsu Y, Tokaji K, Takekawa H. Effect of thick DLC coating on fatigue behaviour of magnesium alloy in laboratory air and demineralised water. Fatigue Fract Eng Mater Struct 2010 (no-no).
- [20] Shiri S, Ashtijoo P, Odeshi A, Yang Q. Evaluation of Stoney equation for determining the internal stress of DLC thin films using an optical profiler. Surf Coat Technol 2016;308:98–100.
- [21] Tillmann W, Hoffmann F, Momeni S, Heller R. Hydrogen quantification of magnetron sputtered hydrogenated amorphous carbon (a-C:H) coatings produced at various bias voltages and their tribological behavior under different humidity levels. Surf Coat Technol 2011;206:1705–10.
- [22] Chhowalla M, Robertson J, Chen CW, Silva SRP, Davis CA, Amaratunga GAJ, et al. Influence of ion energy and substrate temperature on the optical and electronic properties of tetrahedral amorphous carbon (ta-C) films. J Appl Phys 1997;81: 139-45.
- [23] Nakao S, Yukimura K, Nakano S, Ogiso H. DLC coating by HiPIMS: the influence of substrate bias voltage. IEEE Trans Plasma Sci 2013;41:1819–29.
- [24] Dai W, Zheng H, Wu G, Wang A. Effect of bias voltage on growth property of Cr-DLC film prepared by linear ion beam deposition technique. Vacuum 2010;85: 231–5.
- [25] Andersson M, Högström J, Urbonaite S, Furlan A, Nyholm L, Jansson U. Deposition and characterization of magnetron sputtered amorphous Cr–C films. Vacuum 2012; 86:1408–16.
- [26] Huang Z, Chen Z, Lang W, Wang X. Adhesion studies of CrC/a-C:H coatings deposited with anode assisted reactive magnetron sputtering combined with DCpulsed plasma enhanced chemical vapor deposition. Materials 2021:14.
- [27] Casiraghi C, Ferrari AC, Robertson J. Raman spectroscopy of hydrogenated amorphous carbons. Phys Rev B 2005:72.
- [28] Paik N. Raman and XPS studies of DLC films prepared by a magnetron sputter-type negative ion source. Surf Coat Technol 2005;200:2170–4.
- [29] Casiraghi C, Piazza F, Ferrari AC, Grambole D, Robertson J. Bonding in hydrogenated diamond-like carbon by Raman spectroscopy. Diam Relat Mater 2005;14:1098–102.
- [30] Robertson J. The deposition mechanism of diamond-like a-C and a-C: H. Diam Relat Mater 1994;3:361–8.
- [31] Lifshitz Y, Kasi SR, Rabalais JW. Subplantation model for film growth from hyperthermal species: application to diamond. Phys Rev Lett 1989;62:1290–3.
- [32] Zhou X, Tunmee S, Suzuki T, Phothongkam P, Kanda K, Komatsu K, et al. Quantitative NEXAFS and solid-state NMR studies of sp 3 /(sp 2 + sp 3) ratio in the hydrogenated DLC films. Diam Relat Mater 2017;73:232–40.
- [33] Deng J, Braun M. Residual stress and microhardness of DLC multilayer coatings. Diam Relat Mater 1996;5:478–82.
- [34] Foong YM, Koh ATT, Chua DHC. Experimental and theoretical study on the energy-dependent surface evolution and microstructure changes in copper nanostructured composites. J Phys D Appl Phys 2011:44.
- [35] Wang Y, Ye Y, Li H, Ji L, Chen J, Zhou H. A magnetron sputtering technique to prepare a-C:H films: effect of substrate bias. Appl Surf Sci 2011;257:1990–5.
- [36] Mérel P, Tabbal M, Chaker M, Moisa S, Margot J. Direct evaluation of the sp3 content in diamond-like-carbon films by XPS. Appl Surf Sci 1998;136:105–10.
- [37] Tokoroyama T, Hattori T, Umehara N, Kousaka H, Manabe K, Kishi M, et al. Ultralow friction properties of carbon nitride tantalum coatings in the atmosphere. Tribology Int 2016;103:388–93.
- [38] Diaz J, Paolicelli G, Ferrer S, Comin F. Separation of the sp(3) and sp(2) components in the C1s photoemission spectra of amorphous carbon films. Phys Rev B 1996;54:8064–9.
- [39] Jiang J, Wang Q, Huang H, Wang Y, Zhang X, Hao J. Microstructure and property changes induced by substrate rotation in titanium/silicon dual-doped a-C:H films deposited by mid-frequency magnetron sputtering. Surf Coat Technol 2014;240: 419–24.
- [40] Rybachuk M, Bell JM. The effect of sp2 fraction and bonding disorder on micromechanical and electronic properties of a-C:H films. Thin Solid Films 2007;515: 7855–60.
- [41] Sheeja D, Tay BK, Lau SP, Shi X. Tribological properties and adhesive strength of DLC coatings prepared under different substrate bias voltages. WEAR 2001;249: 433–9.
- [42] Kayani A, Moore A, Nandasiri MI, AlFaify S, Garratt E, Ingram D, et al. Effect of bias and hydrogenation on the elemental concentration and the thermal stability of amorphous thin carbon films, deposited on Si substrate. Diam Relat Mater 2009;18: 1333-7.
- [43] Zhang TF, Xie D, Huang N, Leng Y. The effect of hydrogen on the tribological behavior of diamond like carbon (DLC) coatings sliding against Al 2 O 3 in water environment. Surf Coat Technol 2017;320:619–23.
- [44] Sun S, Wang Y, Lu X, Lu X, Mao C, Zeng Z, et al. Achieving excellent tribological performance of a-C: WC film by controlling sub-nano-structure. Tribology Int 2018; 128:65–74.
- [45] Wang J, Li X, Wu G, Lu Z, Zhang G, Xue Q. Origin of low friction for amorphous carbon films with different hydrogen content in nitrogen atmosphere. Tribology Int 2019:140.

- [46] Andersson J, Erck RA, Erdemir A. Friction of diamond-like carbon films in different atmospheres. Wear 2003;254:1070–5.
- [47] Schall JD, Gao GT, Harrison JA. Effects of adhesion and transfer film formation on the tribology of self-mated DLC contacts. J Phys Chem C 2010;114:5321–30.
- [48] Zhang J, Wang Y, Chen Q, Su YX, Xu JX, Ootani Y, et al. Graphitization dynamics of DLC under water lubrication revealed by molecular dynamics simulation. J Comput Chem Jpn 2019;18:103–4.
- [49] Qi Y, Konca E, Alpas AT. Atmospheric effects on the adhesion and friction between non-hydrogenated diamond-like carbon (DLC) coating and aluminum – a first principles investigation. Surf Sci 2006;600:2955–65.
- [50] Suzuki M, Ohana T, Tanaka A. Tribological properties of DLC films with different hydrogen contents in water environment. Diam Relat Mater 2004;13:2216–20.
- [51] Li L, Guo P, Liu L-L, Li X, Ke P, Wang A. Structural design of Cr/GLC films for high tribological performance in artificial seawater: Cr/GLC ratio and multilayer structure. J Mater Sci Technol 2018;34:1273–80.
- [52] Wang HQ, Zhou Q, Ou YX, Liao B, Zhang X, Hua QS, et al. Tribocorrosion behaviors of nc-TiC/a-C:H nanocomposite coatings: In-situ electrochemical response. Thin Solid Films 2021;730:138719.
- [53] Stern M, Geary AL. Electrochemical polarization.1. A theoretical analysis of the shape of polarization curves. J Electrochem Soc 1957;104:56–63.

- [54] de Freitas Cunha Lins V, de Andrade Reis GF, de Araujo CR, Matencio T. Electrochemical impedance spectroscopy and linear polarization applied to evaluation of porosity of phosphate conversion coatings on electrogalvanized steels. Appl Surf Sci 2006;253:2875–84.
- [55] Wei J, Guo P, Liu L, Li H, Li H, Wang S, et al. Corrosion resistance of amorphous carbon film in 3.5 wt% NaCl solution for marine application. Electrochim Acta 2020;346.
- [56] von Keudell A, Schwarz-Selinger T, Jacob W. Simultaneous interaction of methyl radicals and atomic hydrogen with amorphous hydrogenated carbon films. J Appl Phys 2001;89:2979–86.
- [57] Khun NW, Liu E, Zeng XT. Corrosion behavior of nitrogen doped diamond-like carbon thin films in NaCl solutions. Corros Sci 2009;51:2158–64.
- [58] Liang C-H, Huang C-F, Tsai H-Y. The influence of substrate bias voltages on structure, mechanical properties and anti-corrosion performance of Cr doped diamond-like carbon films deposited by steered cathodic arc evaporation. Thin Solid Films 2015;597:88–96.
- [59] Palomäki T, Wester N, Caro MA, Sainio S, Protopopova V, Koskinen J, et al. Electron transport determines the electrochemical properties of tetrahedral amorphous carbon (ta-C) thin films. Electrochim Acta 2017;225:1–10.
- [60] Choi J, Nakao S, Kim J, Ikeyama M, Kato T. Corrosion protection of DLC coatings on magnesium alloy. Diam Relat Mater 2007;16:1361–4.